

# SINGLE $W$ BOSON PRODUCTION IN HIGH ENERGY $e\gamma$ COLLISIONS

Stephen Godfrey and K. Andrew Peterson

*Ottawa-Carleton Institute for Physics*

*Department of Physics, Carleton University, Ottawa CANADA, K1S 5B6*

We studied single  $W$  boson production in high energy  $e\gamma$  collisions and the sensitivity of various observables to the  $WW\gamma$  gauge boson coupling. We evaluated the helicity amplitudes including the  $W$  decay to final state fermions and all Feynman diagrams which give the same final state. At high energy, the non-resonant diagrams give significant contributions to the cross sections and should not be neglected. We first considered a  $\sqrt{s} = 120$  GeV  $e^+e^-$  collider converted to an  $e\gamma$  collider by backscattering a low energy laser off of one of the original electron beams. Such a collider could measure  $\kappa_\gamma$  to  $\simeq \pm 0.09$  at 95% C.L. which is the same level of precision as could be achieved at LEP200 using  $W$  pair production. We next considered single  $W$  production at a 200 GeV  $e^+e^-$  collider in the Weizacker-Williams approximation which can measure the  $WW\gamma$  vertex independently of the  $WWZ$  vertex. This process can measure  $\kappa_\gamma$  to  $\pm 0.15$  at 95% C.L. which is comparable to the  $W$  pair production process. Finally, we examined  $W$  production at 500 GeV and 1 TeV  $e^+e^-$  colliders, comparing results for photon spectra obtained from a backscattered laser and from beamstrahlung radiation. Here we found that the couplings could best be measured using the backscattered laser photons with  $|\delta\kappa_\gamma| \leq 0.07$  and  $|\lambda_\gamma| \leq 0.05$  at a 500 GeV collider and  $|\lambda_\gamma| \leq 0.02$  at a 1 TeV collider, all at 95% C.L.. These measurements of  $\kappa_\gamma$  and  $\lambda_\gamma$  are as good as can be achieved by direct measurement

at any other facility considered so far and the measurement of  $\kappa_\gamma$  is at the threshold of being able to measure loop contributions to the trilinear gauge boson vertex.

PACS numbers: 12.15.Ji, 14.80.Er, 12.50.Fk

## I. INTRODUCTION

Despite the fact that the standard model of the electroweak interactions [1] agrees extraordinarily well with all existing measurements [2,3] there is a widespread conviction that it is nothing more than a low energy limit of a more fundamental theory [4]. An approach which is receiving growing attention is to represent new physics by additional terms in an effective Lagrangian expansion and then to constrain the coefficients of the effective Lagrangian by precision experimental measurements [4,5,6]. The bounds obtained on the coefficients can then be related to possible theories of new physics. For example, this approach has been used by a number of authors to bound dimension four operators which can contribute to the vacuum polarization tensors of the massive gauge bosons via a global analysis of neutral current data [7]. These bounds have put severe constraints on technicolour theories of dynamical symmetry breaking. Similarly, the trilinear gauge boson couplings have been described by effective Lagrangians [8,9]. In one commonly used parametrization, for on shell photons, the CP and P conserving  $\gamma WW$  vertex is parametrized in terms of two parameters,  $\kappa_\gamma$  and  $\lambda_\gamma$  [8]. Although bounds can be extracted from high precision low energy measurements and measurements at the  $Z^0$  pole, there are ambiguities and model dependencies in the results [10]. In contrast, gauge boson production at colliders can measure the gauge boson couplings directly and unambiguously. The direct measurement of these parameters is at present very weak, with the most constraining limits coming from the UA2 experiment which gives  $-5.4 < \kappa_\gamma < 7.9$  and  $-5.8 < \lambda_\gamma < 5.7$  at 95% C.L. [11]. Putting tight constraints on the trilinear gauge boson couplings is one of the primary motivations for the LEP200 upgrade [8,12,13,14]. The Tevatron and HERA will also be able to measure these vertices [15,16] but precise direct measurement to the level of several percent will have to wait until the era of SSC and LHC [14,17].

Recently, the idea of constructing  $e\gamma$  and  $\gamma\gamma$  colliders using either high energy photons from lasers backscattered off of a high energy electron beam [18] or photons arising from beamstrahlung radiation [19,20,21] has received serious attention. The physics possibilities

for  $e\gamma$  colliders are the subject of a growing literature [22]. In particular, the properties of  $W$  bosons, including the  $\gamma WW$  coupling, has been examined in a number of recent publications. [23,24,25,26]

In this paper we reexamine the sensitivity to which the  $\gamma WW$  vertex can be measured at  $e\gamma$  colliders using photon spectra produced from backscattered lasers, beamstrahlung radiation, and the Weizacker-Williams effective photon approximation. In contrast to other analysis [24,25] we include the decay of the  $W$  boson to final state fermions along with contributions to the final state that do not proceed via an intermediate  $W$  boson. At high energy this provides additional information off the  $W$  resonance through the interference of the various diagrams.

We begin by reexamining the  $\sqrt{s} = 100$  GeV collider which was previously studied assuming a delta function photon spectrum with the photon energy equal to that of the original electron beam. Here we include a realistic backscattered laser spectrum. We next consider single  $W$  production at a 200 GeV  $e^+e^-$  collider as a competing process to  $W$  pair production. Finally we consider  $W$  production at 500 GeV and 1 TeV  $e^+e^-$  colliders and compare the sensitivities achievable using a backscattered laser photon spectrum and a beamstrahlung photon spectrum.

In the next section we write down the effective vertex and the resulting Feynman rule. In Sec. III we present our calculation and results and in the final section we give our conclusions.

## II. THE $WW\gamma$ EFFECTIVE VERTEX

Within the standard model the  $WW\gamma$  vertex is uniquely determined by  $SU(2)_L \times U(1)$  gauge invariance so that a precise measurement of the vertex poses a severe test of the gauge structure of the theory. The most general  $WW\gamma$  vertex, consistent with Lorentz invariance, can be parametrized in terms of seven form factors when the  $W$  bosons couple to essentially massless fermions which effectively results in  $\partial_\mu W^\mu = 0$  [8,9]. For on shell photons, electromagnetic gauge invariance further restricts the tensor structure of the  $WW\gamma$

vertex to allow only four free parameters, two of which violate CP invariance. Measurement of the neutron electric dipole moment constrains the two CP violating parameters,  $\tilde{\kappa}_\gamma$  and  $\tilde{\lambda}_\gamma$ , to values too small to give rise to observable effects in the process we are considering;  $|\tilde{\kappa}_\gamma|, |\tilde{\lambda}_\gamma| < \mathcal{O}(10^{-4})$  [27,28]. Therefore, the most general Lorentz and CP invariant vertex compatible with electromagnetic gauge invariance is commonly parametrized as [8]:

$$\mathcal{L}_{WW\gamma} = -ie \left\{ (W_{\mu\nu}^\dagger W^\mu A^\nu - W_\mu^\dagger A_\nu W^{\mu\nu}) + \kappa_\gamma W_\mu^\dagger W_\nu F^{\mu\nu} + \frac{\lambda_\gamma}{M_W^2} W_{\lambda\mu}^\dagger W_\nu^\mu F^{\nu\lambda} \right\} \quad (1)$$

where  $A^\mu$  and  $W^\mu$  are the photon and  $W^-$  fields,  $W_{\mu\nu} = \partial_\mu W_\nu - \partial_\nu W_\mu$  and  $F_{\mu\nu} = \partial_\mu A_\nu - \partial_\nu A_\mu$  denote the  $W$  and photon field strength tensors, and  $M_W$  is the  $W$  boson mass. Higher dimension operators correspond to momentum dependence in the form factors. The first term, referred to as the minimal coupling term, simply reflects the charge of the  $W$ . The Feynman rule for the  $WW\gamma$  vertex resulting from eqn. (1) is given by:

$$\begin{aligned} ie \{ & g_{\alpha\beta} [(1 - \hat{\lambda} k_- \cdot q) k_{+\mu} - (1 - \hat{\lambda} k_+ \cdot q) k_{-\mu}] \\ & - g_{\alpha\mu} [(1 - \hat{\lambda} k_- \cdot q) k_{+\beta} - (\kappa - \hat{\lambda} k_+ \cdot k_-) q_\mu] \\ & - g_{\beta\mu} [(\kappa - \hat{\lambda} k_- \cdot k_+) q_\alpha - (1 - \hat{\lambda} k_+ \cdot q) k_{-\alpha}] \\ & + \hat{\lambda} (k_{+\mu} k_{-\alpha} q_\beta - k_{-\mu} q_\alpha k_{+\beta}) \} \end{aligned} \quad (2)$$

with the notation and conventions given in Fig. 1 and where  $\hat{\lambda} = \lambda/M_W^2$ . At tree level the standard model predicts  $\kappa_\gamma = 1$  and  $\lambda_\gamma = 0$ . Other parametrizations exist in the literature such as the chiral Lagrangian expansion and one can map the parameters we use to those used in other approaches [5].

Before proceeding it is useful to comment on what to expect for  $\kappa_\gamma$  and  $\lambda_\gamma$ . From the chiral Lagrangian approach one expects that  $\delta\kappa_\gamma \sim \mathcal{O}(10^{-2})$  and  $\lambda_\gamma$  is suppressed by an additional factor of 100 [5]. These order of magnitude estimates are confirmed by explicit calculation. The contribution of the  $t$ -quark results in  $\delta\kappa \simeq 1.5 \times 10^{-2}$  and  $\lambda_V \simeq +2.5 \times 10^{-3}$  while a SM Higgs boson of mass 200 GeV contributes  $\delta\kappa \simeq 5 \times 10^{-4}$  and  $\lambda \simeq 4 \times 10^{-5}$  [29]. Technicolour theories give  $\delta\kappa_Z = -0.023$  and  $\delta\kappa_\gamma = 0$  [6] and supersymmetric theories give  $\delta\kappa_{max} \simeq 7 \times 10^{-3}$  and  $\lambda_{max} \simeq 10^{-3}$  [30].

What one gleans from these numbers is that a deviation of more than a couple of percent would be difficult to accomodate in the SM and in general, contributions via loop corrections typically contribute no more than a couple of percent. Although it might be possible to find models that give slightly larger contributions, for example models with  $Z - Z'$  mixing [31] or models with many particles which contribute coherently to loop contributions [32], if deviations much larger than several percent are observed this would signal something very radical such as composite gauge bosons [33]. Since we know of no convincing models of this sort, to probe for new physics via anomalous trilinear gauge boson couplings one must be able to measure the vertex to the level of a few percent.

Deviations from the standard model ( $a = \delta\kappa = \kappa - 1$ ,  $\lambda$ ) lead to amplitudes which grow with energy and therefore violate unitarity at high energy [34,35]. One method of avoiding violation of the unitarity bound is to include a momentum dependence in the form factors,  $a(q_W^2, \bar{q}_W^2, q_\gamma^2 = 0)$ , so that the deviations vanish when either  $|q_W^2|$  or  $|\bar{q}_W^2|$ , the absolute square of the four momentum of the vector bosons, becomes large [35]. We therefore include the form factors

$$a(q_W^2, \bar{q}_W^2, 0) = a_0[(1 + |q_W^2|/\Lambda^2)(1 + |\bar{q}_W^2|/\Lambda^2)]^{-n} \quad (3)$$

where  $\Lambda$  represents the scale at which new physics becomes important and  $n$  is chosen as the minimum value compatible with unitarity. We take  $n = 1$  and  $\Lambda = 1$  TeV in our numerical results. We find that lowering this scale effects our conclusions slightly although if this were the case the new physics should show up elsewhere. Increasing the scale has only a small effect on our results.

### III. CALCULATION AND RESULTS

The Feynman diagrams contributing to the process  $e^- \gamma \rightarrow \nu f \bar{f}$  are given in Fig. 2. The  $WW\gamma$  vertex we are studying contributes via diagram 2b. To preserve electromagnetic gauge invariance and to properly take into account the background processes our calculation

includes all the diagrams of Fig 2 for arbitrary values of  $\kappa_\gamma$  and  $\lambda_\gamma$ . To obtain the cross sections and distributions we used the CALKUL helicity amplitude technique [36] which for completeness we summarize in Appendix A along with the amplitudes corresponding to Fig. 2. Monte Carlo integration techniques are then used to perform the phase space integrals [37]. We treat the photon distributions as structure functions,  $f_{\gamma/e}(x)$  and integrate them with the  $e\gamma$  cross sections to obtain our results:

$$\sigma = \int f_{\gamma/e}(x) \sigma(e\gamma \rightarrow \nu f \bar{f}) dx \quad (4)$$

where  $x$  is the fraction of the original electron energy carried by the photon. For completeness and for the convenience of the interested reader we include the various photon distributions in Appendix B. For our numerical results we take  $\alpha(M_Z) = 1/128$ ,  $M_W = 80.22$  GeV,  $\Gamma_W = 2.0$  GeV,  $\sin^2 \theta_w = 0.23$ .

The signal we are studying consists of either, (i) for leptonic  $W$  decay, a high transverse momentum lepton ( $p_T$ ) and large missing transverse momentum ( $\cancel{p}_T$ ) due to the neutrinos from the initial electron beam and from the  $W$  decay, or (ii) for hadronic  $W$  decay, two hadronic jets and large missing transverse momentum ( $\cancel{p}_T$ ) due to the neutrino from the initial electron beam. In both cases, we require that visible particles in the final state be at least  $10^\circ$  from the beam direction. Our conclusions are not sensitive to the exact value of this cut. We also impose a cut on the minimum  $\cancel{p}_T$ ; for  $\sqrt{s} = 120$  GeV and 200 GeV we used  $\cancel{p}_T > 5$  GeV and for  $\sqrt{s} = 500$  GeV and 1 TeV we used  $\cancel{p}_T > 10$  GeV. We do not include fragmentation and hadronization effects for the hadronic modes and identify the hadron jet momenta with that of the quarks. The signals we consider are therefore

$$e^- + \gamma \rightarrow \mu^- + \cancel{p} \quad (5)$$

$$e^- + \gamma \rightarrow j + j + \cancel{p} \quad (6)$$

We also examined the reaction  $e^- \gamma \rightarrow e \bar{\nu} \nu$  which includes the process  $e^- \gamma \rightarrow e^- Z^0 \rightarrow e^- \nu \bar{\nu}$  in addition to the diagrams of figure 2. However, once kinematic cuts are imposed that eliminate the uninteresting contributions from  $e\gamma \rightarrow e^- Z$  we are left with results comparable to the  $\mu$  mode.

In the following subsections we study single  $W$  production for  $\sqrt{s} = 120$  GeV, 200 GeV, 500 GeV, and 1 TeV. In doing so we examine a number of kinematic distributions, asymmetries, and ratios of observables for their sensitivity to anomalous gauge boson couplings. Since we will only present results for the observables most sensitive to the gauge boson couplings, at this point we list all observables that we studied. For the leptonic  $W$  decay modes we considered;  $d\sigma/dp_{T\mu}$ ,  $d\sigma/dE_\mu$ ,  $d\sigma/d\cos\theta_{e\mu}$ , where  $\theta_{e\mu}$  is the angle between the incoming electron and the outgoing muon,  $A_{FB} = (\sigma_F - \sigma_B)/(\sigma_F + \sigma_B)$ ,  $R_{IO} = \sigma_I/\sigma$  where  $\sigma_I$  is the cross section for  $|\cos\theta_{e\mu}| < 0.4$  and  $\sigma$  is the total cross section with the kinematic cuts given above. When backscattered laser photons are used we can form the ratio  $R_{13} = \sigma_1/\sigma_3$  where  $\sigma_1$  is the cross section for the mainly helicity 1/2 amplitudes which result when the incident photons are left handed and  $\sigma_3$  is the cross section for the mainly helicity 3/2 amplitudes when the incident photons are right handed<sup>1</sup>. For the hadronic  $W$  decay modes we reconstructed the  $W$  boson 4-momentum from the hadronic jets' 4-momentum, imposing the kinematic cut of  $75 \text{ GeV} < M_{q\bar{q}} = \sqrt{(p_q + p_{\bar{q}})^2} < 85 \text{ GeV}$ . Including the nonresonant diagrams of fig (2c) and (2d) and reconstructing the  $W$  boson in this manner gives different results than from simply studying the cross sections to  $W$  bosons. Finally, in some cases, which we will describe in further detail below, we studied the effect of anomalous couplings on the cross section of the hadronic modes *off* the  $W$  pole (i.e.  $M_{q\bar{q}} \neq M_W$ ). In general, deviations of the gauge boson couplings had a very substantial effect on the cross section off the  $W$  resonance although, because of the reduced cross section, the statistical significance is not really enhanced. This does, however, point out the importance of considering the process that is actually measured, not simply a theorist's idealization.

#### A. $\sqrt{s} = 120$ GeV

In previous papers the  $\sqrt{s} = 100$  GeV  $e\gamma$  collider was examined in detail assuming the photon energy was equal to that of the original electron beam [23]. However when we

---

<sup>1</sup>Note that the high energy photon beam has opposite polarization to that of the laser.



folded in the backscattered photon spectrum, the cross section was reduced by an order of magnitude to 0.03 pb for the muon mode and 0.06 pb for the  $q\bar{q}$  mode, with the cuts described above<sup>2</sup> which yields an event rate too low to perform a useful physics analysis with integrated luminosities of  $O(100)$  pb<sup>-1</sup>. The reason for the reduced cross section is not hard to see; the backscattered photon spectrum peaks at about 0.84 of the original beam energy. For electron beams of 50 GeV this results in  $\sqrt{s} \sim 90$  GeV which is just barely above the  $W$  production threshold where the cross section is still relatively small. We therefore studied the physics potential for an increased beam energy of 60 GeV ( $\sqrt{s} = 120$  GeV), perhaps from a hypothetically upgraded SLC collider. The modest increase in energy results in almost an order of magnitude increase in the cross section; 0.12 pb for the muon mode and 0.53 pb for the hadronic mode with the kinematic cuts we used.

Of the observables listed in the previous section, those involving the reconstructed  $W$  from the hadronic decay modes were the most sensitive to anomalous couplings. This is simply due to the factor of six larger  $W$  branching fraction of the hadronic modes relative to the muon mode. The specific observables found to be most sensitive are the total cross section ( $\sigma_T$ ),  $A_{FB}(W)$ ,  $R_{13}(W)$ , and binning the angular distribution into two bins;  $\sigma_F$  and  $\sigma_B$ . The  $W$  angular distribution for  $e\gamma \rightarrow W\nu \rightarrow q\bar{q}\nu$  is plotted in Fig. 3 with and without the backscattered photon distribution folded in. When the photon spectrum is included the angular distribution is shifted in the forward direction and the radiation zero at  $\cos\theta = 1$  is totally eliminated. In Fig. 4 we show the 95% C.L. contours obtained using  $\sigma_T$  and  $A_{FB}$  based on the statistical errors obtained by assuming 100 pb<sup>-1</sup> and 500 pb<sup>-1</sup> of integrated luminosity. To obtain these curves we calculated the observables for a given value of  $\kappa_\gamma$  and  $\lambda_\gamma$  and determined at what level the value, if measured, would be compatible with the standard model prediction. The central region is the 95% C.L. bound obtainable from the combined measurements. We obtain similar results by combining  $\sigma_F$  and  $\sigma_B$ , the cross

---

<sup>2</sup>The cross sections are very sensitive to the exact values of  $M_W$  and the cuts we used.

sections in the forward and backward directions respectively. The inclusion of  $R_{13}$  would improve the bounds on the right side of the curves (+ve  $\lambda_\gamma$ ) slightly. These results do not depend on whether or not we use the cuts on  $M_{q\bar{q}}$  indicating that the hadronic cross section is dominated by the  $W$  boson pole. Varying one parameter at a time and holding the other fixed at its standard model value we obtain  $\delta\kappa_\gamma = \pm 0.09$  and  $|\lambda_\gamma| \leq 0.8$  at 95% C.L.. The bounds that could be achieved using the various observables are given in Table I. The constraints that could be obtained on  $\kappa_\gamma$  would be comparable to that obtainable at LEP200 but the limits on  $\lambda_\gamma$  would be about a factor of two less stringent.

### B. $\sqrt{s} = 200$ GeV; LEP 200

At LEP 200 the possibility of  $e\gamma$  collisions is only possible via t-channel photon exchange between the electron and positron beams [38]. We therefore examine single  $W$  production in  $e^+e^-$  collisions by folding the cross sections for  $e\gamma \rightarrow q\bar{q}\nu$  and  $e\gamma \rightarrow \mu\bar{\nu}\nu$  with the Weizacker-Williams photon distribution.

As in the  $\sqrt{s} = 120$  GeV case we found that distributions utilizing  $W$ 's reconstructed from the hadronic modes were most sensitive to the  $WW\gamma$  couplings. This is primarily due to the increased statistics of the hadronic modes over the leptonic modes since the bounds obtained at 200 GeV are limited by statistics;  $\sigma_\mu = 0.059$  pb vs  $\sigma_W = 0.28$  pb (with the cut on  $M_{q\bar{q}}$ ). We found that deviations in the total cross section and the angular distribution of the reconstructed  $W$  gave the greatest sensitivity to anomalous couplings. In Fig. 5 we show the angular distribution of the reconstructed  $W$ 's. To obtain sensitivity bounds we used the total cross section and  $A_{FB}$  of the reconstructed  $W$  boson. The 95% C.L. limits are given in Fig. 6 along with the combined bounds. As in the  $\sqrt{s} = 120$  GeV case the “binned”  $\sigma_F$  and  $\sigma_B$  gives almost identical constraints. The 95% C.L. limits obtained by varying one parameter at a time, for  $L = 500$  pb $^{-1}$ , are  $0.85 < \kappa_\gamma < 1.13$  and  $-0.63 < \lambda_\gamma < 0.61$  from  $\sigma(e^+e^- \rightarrow e^+W^-)$ . The bounds that could be achieved using the different observables are listed in Table II. The sensitivity on  $\kappa_\gamma$  is comparable to that obtained from the  $W$ -pair production process but offers a means of measuring the  $WW\gamma$  vertex independently of the

$WWZ$  vertex and is therefore an important complement to the  $W$ -pair production process.

Another possible kinematic variable is the  $q\bar{q}$  invariant mass,  $M_{q\bar{q}}$  which we plot in Fig. 7 for representative values of  $\kappa_\gamma$  and  $\lambda_\gamma$ . At the high mass regions the deviations are at least comparable to the deviations at the  $W$ -pole. The cross section is, however, too small to yield useful statistics, at least in the Weizacker-Williams approximation. Calculating the single  $W$  production cross section exactly, and including all the diagrams contributing to the same final state appears to offer an increase in the cross section in the high mass region and is undergoing detailed investigation which will appear elsewhere [39]. The important point is that the normally neglected nonresonant diagrams which contribute to the final state can, and often do, make a non-negligible contribution to the cross section and should not be neglected.

### C. The Next Linear Collider; $\sqrt{s} = 500$ GeV and $\sqrt{s} = 1000$ GeV

For the NLC [40] we consider two possibilities for the photon spectrum; that arising from backscattering a laser from one of the original electron beams and beamstrahlung, which is the radiation which arises when two intense beams of electrons pass through one another. For the results using the beamstrahlung photon spectrum we concentrate on the beam spectrum resulting from the G set of parameters of Ref. [41]. We will discuss the effect of different beam parameters on our results. We included the Weizacker-Williams contributions in our beamstrahlung results.

The NLC is envisaged as a very high luminosity collider so that the number of events per unit of  $R$ , the QED point cross section, which is an s-channel process and goes like  $1/s$ , remains reasonable. The integrated luminosities for a Snowmass year ( $10^7$  sec) are expected to be  $\sim 60 \text{ fb}^{-1}$  for a  $\sqrt{s} = 500$  GeV collider and  $\sim 200 \text{ fb}^{-1}$  for a  $\sqrt{s} = 1$  TeV collider. Typical cross sections for the process  $e\gamma \rightarrow \mu\bar{\nu}_\mu\nu_e$  and  $e\gamma \rightarrow W\nu \rightarrow q\bar{q}\nu$  at  $\sqrt{s} = 500$  GeV are 3.2 pb and 16.6 pb respectively for the backscattered laser mode and 2.1 pb and 10.8 pb respectively for the beamstrahlung mode, leading to  $\sim 10^6$  events per year. At  $\sqrt{s} = 1$  TeV  $\sigma(e\gamma \rightarrow \mu\bar{\nu}_\mu\nu_e) = 4.0$  pb and  $\sigma(e\gamma \rightarrow W\nu \rightarrow q\bar{q}\nu) = 19$  pb for the

backscattered laser mode and  $\sigma(e\gamma \rightarrow \mu\bar{\nu}_\mu\nu_e) = 6.0$  pb and  $\sigma(e\gamma \rightarrow W\nu \rightarrow q\bar{q}\nu) = 31$  pb for the beamstrahlung mode leading to  $\sim 6 \times 10^6$  events/year. Thus, except for certain regions of phase space, the errors are not limited by statistics, but rather by systematic errors. Factors entering into systematic errors include an accurate knowledge of the total luminosity, particle misidentification, triggering and detector efficiencies, uncertainty in the size of backgrounds, calorimetric accuracy etc. Estimating systematic errors requires detailed Monte Carlo studies which we do not attempt. For cross sections we assume a systematic error of 5% and for asymmetries and ratios, where some of the systematic errors cancel, we assume a systematic error of 3% [42]. We consider the effects of reducing these systematic errors on the achievable sensitivities. In our results we combine in quadrature the statistical errors based on the integrated luminosities given above with the systematic errors:

$$\delta^2 = \delta_{stat}^2 + \delta_{sys}^2. \quad (7)$$

We begin with  $\sqrt{s} = 500$  GeV. As in the previous cases for  $\sqrt{s} = 120$  GeV and  $\sqrt{s} = 200$  GeV the total cross sections and the angular distributions of the outgoing muon and reconstructed  $W$  are sensitive to anomalous couplings. We plot the distributions for both the backscattered photon case and the beamstrahlung case in Fig. 8. At higher energies we can obtain additional information, especially for  $\lambda_\gamma$ , from the  $p_T$  spectrum of the outgoing lepton or the reconstructed  $W$ . We show these spectra in Fig. 9. Finally, as already pointed out, the invariant mass distribution, shown in Fig. 10, of the  $q\bar{q}$  pair above the  $W$  mass also provides useful information. If, for example, we integrate the  $M_{q\bar{q}}$  spectrum from 100 GeV up, we obtain a cross section of 0.25 pb for the backscattered laser mode which offers considerable statistics. For  $M_{q\bar{q}} > 300$  GeV,  $\sigma = 0.006$  pb which yields  $\sim 400$  events/year. More importantly, this high  $M_{q\bar{q}}$  region shows a higher sensitivity to anomalous couplings than the  $M_W$  pole region.

To quantify the observations of the above paragraph we consider the cross sections, the angular distributions, and the  $p_T$  distributions for the muon and hadronic modes and the hadronic cross section for  $M_{q\bar{q}} > 300$  GeV. For the angular distributions we used four equal

bins and for the  $p_T$  distributions we used the 4  $p_T$  bins; 0 – 100 GeV, 100-150 GeV, 150-200 GeV, and 200-250 GeV. The bounds obtained for these observables are shown in Fig. 11 based on systematic errors of 5%. Bounds obtained by varying one parameter at a time are summarized in Table III. In general the limits on  $\kappa_\gamma$  obtained using the beamstrahlung spectrum are comparable to those obtained from the backscattered photon spectrum. The bounds on  $\lambda_\gamma$  are tighter using the backscattered laser photons which reflects the harder photon spectrum in this case to which  $\lambda_\gamma$  is more sensitive. We find that  $\kappa_\gamma$  can be measured to within 7% and  $\lambda_\gamma$  to within  $\pm 0.05$  at 95% C.L., using the backscattered laser approach, which is approaching the sensitivity required to observe the contributions of new physics at the level of loop corrections.

Unlike the case at lower energies, the limits from the muon mode and reconstructed  $W$  mode are comparable. This is due to two reasons: First, while the  $W$  mode is restricted to the small portion of the phase space at the  $W$  mass. In contrast, the muon mode reflects the entire kinematically allowed region, in particular the highest energy region where deviations from the standard model are most pronounced. Although the diagram we are interested in does not dominate in this higher energy region, the interference between it and the non-resonant diagrams are important. Once again, this underlines the importance of considering all contributions to the process that will actually be observed and only then impose constraints. Furthermore, because of the large expected integrated luminosities the errors are dominated by systematic errors so that the differences between the hadronic and leptonic branching fractions become unimportant.

We repeat the above exercise for  $\sqrt{s} = 1$  TeV using an integrated luminosity of  $200 \text{ fb}^{-1}$ . As was the case at 500 GeV we find that the angular and  $p_{T_W}$  distributions give the best constraints on anomalous couplings. These distributions are shown in Fig. 12 and 13 and are seen to be qualitatively similar to the 500 GeV distributions. The invariant mass distributions of the  $q\bar{q}$  pair is very similar to the 500 GeV except that it extends out about a factor of two further. To extract bounds from these distributions we divided the angular distributions into four equal bins and the  $p_{T_W}$  distribution into the four bins; 0 – 200 GeV,

200-300 GeV, 300-400 GeV, and 400-500 GeV. At 1 TeV there is little improvement on the sensitivity to  $\kappa_\gamma$  and about a factor of two improvement on the sensitivity to  $\lambda_\gamma$  resulting in a possible limit of  $\delta\lambda_\gamma = \pm 0.016$  at 95% C.L. using the laser mode. This measurement improvement on  $\lambda_\gamma$  reflects the greater sensitivity at higher energy. Confidence level curves are shown in Fig. 14 with some of the results summarized in Table IV.

To obtain these sensitivities to anomalous couplings we made a number of assumptions on  $\Lambda$ , the scale of new physics used in the form factors, the beamstrahlung spectrum, and the systematic error. We discuss the effects of varying these parameters starting with the systematic error which is relevant to the 500 GeV and 1 TeV cases. Reducing the systematic error from 5% to 2% reduces the precision on  $\kappa_\gamma$  roughly proportionately with the systematic error, i.e. a factor of two reduction in the systematic error will tighten the limits on  $\kappa_\gamma$  by roughly a factor of two. In contrast, the attainable constraints on  $\lambda_\gamma$  does not in general improve as much, especially for constraints obtained from the  $p_{TW}$  distributions which give the tightest of all bounds on  $\lambda_\gamma$ . This is more pronounced for the 500 GeV case than the TeV case. We can see the reason for this by referring to figures 8, 9, 12, and 13. Varying  $\kappa_\gamma$  results in an overall shift in the cross section effecting all regions of phase space while in contrast, the effect of  $\lambda_\gamma$  grows larger with increasing  $p_{TW}$ . The largest effect is at highest  $p_T$  where the cross section, and hence the statistics are lowest. Thus, at least for the 500 GeV case, statistical errors still play a role and it indicates that at a TeV they could also be important if the NLC does not achieve the large integrated luminosities we have assumed.

We next consider the effect of using the beamstrahlung spectrum arising from the G=1 beam geometry. The only place this change has any effect on our results is a slight improvement on the bounds obtained using the  $p_T$  distributions. This can be attributed to the effect the harder photon spectrum has on the  $p_T$  distribution.

Finally, we consider the effect of varying  $\Lambda$ , the energy scale used in the form factors to preserve unitarity at high energy. We took  $\Lambda = 1$  TeV to obtain our results. Changing  $\Lambda$  to 500 GeV and to 2 TeV has no effect whatsoever on our  $\sqrt{s} = 120$  GeV and 200 GeV bounds. For the 500 GeV case there is a small decrease in the sensitivity (of the order of

a few percent) if we decrease  $\Lambda$  to 500 GeV and virtually no change when we increase it to 2 TeV. This is true for all measurements except those involving the  $p_T$  distribution. This is not unexpected. Since the form factor was introduced to suppress anomalous couplings at high energy, if the cutoff scale is reduced it is doing what it was introduced to do. If this scale is much larger than the characteristic energy scale of the process being studied, increasing it further should have no effect. The exception of the  $p_T$  distributions reflects that these particular observables are most sensitive to deviations at high energy. We find similar effects for the  $\sqrt{s} = 1$  TeV collider although here the changes are more pronounced. To demonstrate the effect on the  $p_T$  distribution we plot in Fig. 15 the  $p_T$  distribution of the outgoing muon for the three values of  $\Lambda$  with  $\lambda_\gamma = 0.1$  using the backscattered laser spectrum with  $\sqrt{s} = 1$  TeV. We do not consider the choice of this scale an important one. If it were small enough to make a difference in these measurements we would expect the new physics to manifest itself in other ways, otherwise, the scale would be large enough not to matter.

#### IV. CONCLUSIONS

We examined single  $W$  production in  $e\gamma$  collisions for a number of collider energies and sources of energetic photons. In our studies we included the  $W$  boson decays to final state fermions and other processes which contribute to the same final state. At high energy, the off resonance results are important since interference effects between these other diagrams and the  $W$  production diagrams enhance the significance of anomalous couplings, particularly  $\lambda_\gamma$ . Although these effects contribute relatively little to the total cross section, their significance in constraining the anomalous couplings can be large, especially at high energies and high luminosities where these effects are statistically significant.

We found that with a  $\sqrt{s} = 120$  GeV  $e^+e^-$  collider operating as an  $e\gamma$  collider,  $\kappa_\gamma$  could be measured to  $\pm 0.09$  at 95% C.L. with  $500 \text{ pb}^{-1}$  which is as good as can be expected using  $W$  pair production at LEP200 and is almost two orders of magnitude more precise than

present direct measurements. On the other hand  $\lambda_\gamma$  can be constrained to  $\pm 0.8$  at 95% C.L. which, although a significant improvement over present measurements, is not as sensitive as the expected LEP200 sensitivity.

We considered single  $W$  production in  $e^+e^-$  collisions at  $\sqrt{s} = 200$  GeV in the effective photon approximation. Here we found that  $\kappa_\gamma$  could be measured to  $\sim \pm 0.15$  and  $\lambda_\gamma$  to  $\sim \pm 0.6$  at 95% C.L.. Again, the former measurement is comparable to what can be achieved in  $W$  pair production while the latter is not quite as precise. What makes this process interesting is that it offers a means of measuring the  $WW\gamma$  couplings independently of the  $WWZ$  couplings which is far from trivial in the  $W$  pair production process. Given the potential importance of this process, an explicit calculation of the reaction  $e^+e^- \rightarrow f_1\bar{f}_2f_3\bar{f}_4$  is in progress that does not resort to the Weizacker-Williams approximation [38,39].

For the high energy, high luminosity, NLC  $e^+e^-$  collider we considered both a backscattered laser photon spectrum and a beamstrahlung photon spectrum. For  $\sqrt{s} = 500$  GeV  $\delta\kappa_\gamma \simeq \pm 0.07$  and  $\delta\lambda_\gamma \simeq \pm 0.05$  and for  $\sqrt{s} = 1$  TeV,  $\delta\kappa_\gamma \simeq \pm 0.07$  and  $\delta\lambda_\gamma \simeq \pm 0.016$  using the backscattered laser approach. Using the beamstrahlung photon spectrum is only slightly less sensitive. The measurement of  $\kappa_\gamma$  is approaching the level of radiative corrections and might be sensitive to new physics at the loop level. On the other hand, it is expected that the sensitivity to  $\lambda$  would have to be at least an order of magnitude more sensitive to be interesting. From our analysis it does not appear that there is any overwhelming advantage to go to higher energies to study the trilinear gauge boson couplings using  $e\gamma$  collisions.

The bounds obtainable for  $\kappa_\gamma$  are at least twice as precise as any obtainable from direct measurement at any other facility being considered — they are roughly twice as sensitive as those achievable at the SSC, and the bounds on  $\lambda_\gamma$  are comparable to those obtainable at the SSC.



## ACKNOWLEDGMENTS

The authors are most grateful to Tim Barklow, Pat Kalyniak, Dean Karlen, Francis Halzen and Paul Madsen for helpful conversations and to Concha Gonzalez-Garcia for helpful communications. This research was supported in part by the Natural Sciences and Engineering Research Council of Canada.

## APPENDIX A: HELICITY AMPLITUDES

In this appendix, we summarize the CALKUL spinor technique [36] and give the helicity amplitudes for the process  $e\gamma \rightarrow \nu f \bar{f}'$  where  $f\bar{f}'$  can be  $\mu\bar{\nu}_\mu$  or  $q\bar{q}'$ . We do not go into any detail and refer the interested reader to the literature and references therein. We limit our discussion to massless fermions and massless external gauge bosons, which apply to our problem. The propagators for the fermions and gauge bosons have the same form as in the usual trace technique so we will not discuss them here.

The spinor technique results in reducing strings of spinors and gamma matrices to sandwiches of spinors which can be evaluated easily. In doing so, one makes extensive use of the *right* and *left* projection operators defined by  $\omega_\pm = \frac{1}{2}(1 \pm \gamma_5)$ . One defines two four-vectors,  $k_0^\mu$  and  $k_1^\mu$ , which obey the following relations:

$$k_0 \cdot k_0 = 0, \quad k_1 \cdot k_1 = -1, \quad k_0 \cdot k_1 = 0.$$

and the basic spinors:

$$u_-(k_0)\bar{u}_-(k_0) = \omega_- \not{k}_0$$

and

$$u_+(k_0) = \not{k}_1 u_-(k_0)$$

Note that in the massless limit, one can use  $u$  and  $\bar{u}$  to describe both particles and antiparticles, with the spin sum  $\sum_\lambda u_\lambda(p)\bar{u}_\lambda(p) = \not{p}$ . These two spinors are the building blocks for

any spinor of lightlike momentum  $p$  :

$$u_\lambda(p) = \frac{\not{p} u_{-\lambda}(k_0)}{\sqrt{2} p \cdot k_0}$$

Two identities are essential for the reduction of the strings; the spin sum given above and the Chisholm identity:

$$\bar{u}_\lambda(p_1) \gamma^\mu u_\lambda(p_2) \gamma_\mu \equiv 2u_\lambda(p_2) \bar{u}_\lambda(p_1) + 2u_{-\lambda}(p_1) \bar{u}_{-\lambda}(p_2)$$

where  $\lambda$  is  $\pm 1$  and represents the helicity state. These two identities allow one to reduce strings of spinors and gamma matrices to sandwiches of spinors. Only two of the four possible sandwiches are non-zero:

$$s(p_1, p_2) \equiv \bar{u}_+(p_1) u_-(p_2) = -s(p_2, p_1)$$

and

$$t(p_1, p_2) \equiv \bar{u}_-(p_1) u_+(p_2) = s(p_2, p_1)^*.$$

Once the amplitude has been reduced to a series of factors of  $s(p_i, p_j)$  and  $t(p_k, p_l)$ , the expressions can be evaluated by computer. A judicious choice of the four-vectors  $k_0^\mu$  and  $k_1^\mu$  simplifies the evaluation of the  $s$  and  $t$  terms. For our calculation, we used the definition of ref. [36];

$$p_i^\mu = (p_i^0, p_i^x, p_i^y, p_i^z)$$

$$k_0^\mu = (1, 1, 0, 0)$$

$$k_1^\mu = (0, 0, 1, 0)$$

to obtain

$$s(p_1, p_2) = (p_1^y + ip_1^z) \frac{\sqrt{p_2^0 - p_2^x}}{\sqrt{p_1^0 - p_1^x}} - (p_2^y + ip_2^z) \frac{\sqrt{p_1^0 - p_1^x}}{\sqrt{p_2^0 - p_2^x}}$$

These forms are ideally suited for programming. When dealing with several diagrams, one simply evaluates the amplitudes of each diagram as complex numbers and squares the sum of the amplitudes in order to obtain the  $|amplitude|^2$ .

To include massless gauge bosons one represents, as usual, the gauge boson by its polarization vector. Following Kleiss and Sterling we use the definition:

$$\epsilon_\lambda^\mu(k) \equiv \frac{1}{\sqrt{4 p \cdot k}} \bar{u}_\lambda(k) \gamma^\mu u_\lambda(p)$$

where  $p^\mu$  is any lightlike four-vector not collinear to  $k^\mu$  or  $k_0^\mu$ . The choice of  $p^\mu$  acts as a choice of gauge and provides a powerful verification of gauge invariance; it can be shown that two different choices of  $p^\mu$  will lead to two expressions that will differ by a term proportional to the photon momentum. When dotted into the amplitude, this extra term must vanish identically because of gauge invariance. Hence, two different choices of  $p^\mu$  must give exactly the same answer. If they don't, there is a mistake in the amplitude. Generally, we choose  $p^\mu$  to be one of the four-vectors of the problem at hand.

Using this technique we obtain for the helicity amplitudes corresponding to the Feynman diagrams of Fig. 2, using the notation  $M = ie g^2 \tilde{M} / \sqrt{4 p_\gamma \cdot k}$ :

$$\tilde{M}_{LL}^a = -\frac{2}{s P_W(q + \bar{q})} t(p_\nu, q) s(\bar{q}, p_e) t(p_e, p_\gamma) s(k, p_e) \quad (A1)$$

$$\tilde{M}_{LR}^a = -\frac{2}{s P_W(q + \bar{q})} t(p_\nu, q) s(p_\gamma, p_e) [s(\bar{q}, p_e) t(p_e, k) + s(\bar{q}, p_\gamma) t(p_\gamma, k)] \quad (A2)$$

$$\begin{aligned} \tilde{M}_{LL}^b &= \frac{1}{P_W(p_e - p_\nu) P_W(q + \bar{q})} \\ &\times \left\{ -2t(p_\nu, q) s(\bar{q}, p_e) [t(p_\gamma, p_e) s(p_e, k) - t(p_\gamma, p_\nu) s(p_\nu, k)] \right. \\ &\quad + (1 + \kappa + \hat{\lambda}(p_e - p_\nu)^2) t(q, p_\gamma) s(k, \bar{q}) t(p_\nu, p_\gamma) s(p_\gamma, p_e) \\ &\quad - (1 + \kappa + \hat{\lambda}(q + \bar{q})^2) t(p_\nu, p_\gamma) s(k, p_e) t(q, p_\gamma) s(p_\gamma, \bar{q}) \\ &\quad + \hat{\lambda}[t(p_\gamma, p_e) s(p_e, k) - t(p_\gamma, p_\nu) s(p_\nu, k)] \\ &\quad \left. \times t(q, p_\gamma) s(p_\gamma, \bar{q}) t(p_\nu, p_\gamma) s(p_\gamma, p_e) \right\} \quad (A3) \end{aligned}$$

$$\begin{aligned} \tilde{M}_{LR}^b &= \frac{1}{P_W(p_e - p_\nu) P_W(q + \bar{q})} \\ &\times \left\{ -2t(p_\nu, q) s(\bar{q}, p_e) [s(p_\gamma, p_e) t(p_e, k) - s(p_\gamma, p_\nu) t(p_\nu, k)] \right. \\ &\quad + (1 + \kappa + \hat{\lambda}(p_e - p_\nu)^2) t(q, k) s(p_\gamma, \bar{q}) t(p_\nu, p_\gamma) s(p_\gamma, p_e) \\ &\quad - (1 + \kappa + \hat{\lambda}(q + \bar{q})^2) t(p_\nu, k) s(p_\gamma, p_e) t(q, p_\gamma) s(p_\gamma, \bar{q}) \\ &\quad \left. + \hat{\lambda}[s(p_\gamma, p_e) t(p_e, k) - s(p_\gamma, p_\nu) t(p_\nu, k)] \right\} \end{aligned}$$

$$\times t(q, p_\gamma) s(p_\gamma, \bar{q}) t(p_\nu, p_\gamma) s(p_\gamma, p_e) \} \quad (\text{A4})$$

$$\begin{aligned} \tilde{M}_{LL}^c = & + \frac{2Q_{\bar{f}}}{(p_\gamma - \bar{q})^2 P_W(p_e - p_\nu)} \\ & \times t(q, p_\nu) s(k, \bar{q}) [s(p_e, q) t(q, p_\gamma) + s(p_e, p_\nu) t(p_\nu, p_\gamma)] \end{aligned} \quad (\text{A5})$$

$$\begin{aligned} \tilde{M}_{LR}^c = & + \frac{2Q_{\bar{f}}}{(p_\gamma - \bar{q})^2 P_W(p_e - p_\nu)} \\ & \times t(q, p_\nu) s(p_\gamma, \bar{q}) [s(p_e, q) t(q, k) + s(p_e, p_\nu) t(p_\nu, k)] \end{aligned} \quad (\text{A6})$$

$$\begin{aligned} \tilde{M}_{LL}^d = & + \frac{2Q_f}{(q - p_\gamma)^2 P_W(p_e - p_\nu)} \\ & \times t(q, p_\gamma) s(p_e, \bar{q}) [s(k, q) t(q, p_\nu) - s(k, p_\gamma) t(p_\gamma, p_\nu)] \end{aligned} \quad (\text{A7})$$

$$\tilde{M}_{LR}^d = + \frac{2Q_f}{(q - p_\gamma)^2 P_W(p_e - p_\nu)} t(q, k) s(p_e, \bar{q}) s(p_\gamma, q) t(q, p_\nu) \quad (\text{A8})$$

where the propagators are defined by

$$P_W(p) = [p^2 - M_W^2 + i\Gamma_W M_W]. \quad (\text{A9})$$

The first subscript of the amplitudes refers to the helicity of the electron and the second subscript to the helicity of the photon. The amplitudes correspond to the diagrams of Fig. 2 where the four momenta  $p_e, p_\gamma, p_\nu, q$  and  $\bar{q}$  are defined.  $Q_f = Q_d = -1/3$  and  $Q_{\bar{f}} = Q_u = +2/3$ . Helicity amplitudes not explicitly written down are zero. To obtain the cross section the amplitudes for given electron and photon helicities are summed over and squared. These are then averaged to obtain the spin averaged matrix element squared and finally integrated over the final state phase space to yield the cross section.

## APPENDIX B: THE PHOTON DISTRIBUTIONS

To obtain the cross sections in the main text we convolute the  $e\gamma$  cross section with the relevant photon distributions:

$$\sigma = \int_0^1 f_{\gamma/e}(x) \sigma(e\gamma \rightarrow W\nu) dx \quad (\text{B1})$$

where the various photon distributions,  $f_{\gamma/e}(x)$ , are given below.

## 1. Back-Scattered Laser Photons

Intense high energy photon beams can be obtained by backscattering a low energy laser off of a high energy electron beam. The energy spectrum of the back-scattered laser photons is given by [18]

$$f_{\gamma/e}^{laser}(x, \xi) = \frac{1}{D(\xi)} \left[ 1 - x + \frac{1}{1-x} - \frac{4x}{\xi(1-x)} + \frac{4x^2}{\xi^2(1-x)^2} \right] \quad (\text{B2})$$

where the fraction  $x$  represents the ratio of the scattered photon energy,  $\omega$ , and the initial electron energy,  $E$ , ( $x = \omega/E$ ) and

$$D(\xi) = \left( 1 - \frac{4}{\xi} - \frac{8}{\xi^2} \right) \ln(1 + \xi) + \frac{1}{2} + \frac{8}{\xi} - \frac{1}{2(1 + \xi)^2} \quad (\text{B3})$$

with

$$\xi = \frac{4E\omega_0}{m_e^2} \cos^2 \frac{\alpha_0}{2} \simeq \frac{2\sqrt{s}\omega_0}{m_e^2} \quad (\text{B4})$$

and  $\omega_0$  is the laser photon energy and  $\alpha_0 \sim 0$  is the electron-laser collision angle. The maximum value of  $x$  is

$$x_m = \frac{\omega_m}{E} = \frac{\xi}{(1 + \xi)}. \quad (\text{B5})$$

Because of the onset of  $e^+e^-$  pair production between backscattered and laser photons, conversion efficiency drops considerably for  $x > 2 + 2\sqrt{2} \approx 4.82$ . We use this value which for 250 GeV electrons corresponds to a laser energy of about 1.26 eV.

The photon spectrum is sensitive to the the product  $\lambda_e P_\gamma$  where  $\lambda_e$  is the mean electron helicity and  $P_\gamma$  is the mean laser helicity. Larger values of  $\lambda_e P_\gamma$  give a harder more monochromatic photon spectrum. Measuring the actual  $\lambda_e$  introduces systematic errors so we assume that the electron beam is unpolarized. In constrast the laser can be easily polarized almost completely. The amount of polarization is energy dependent. Assuming  $P_\gamma = 1$  the average helicity  $\xi_2$  of the photon beam is given by

$$\xi_2 = -\frac{\xi(\xi - 2x - \xi x)(2 - 2x + x^2)}{2\xi^2 - 4x\xi - 4\xi^2 x + 4x^2 + 4\xi x^2 + 3\xi^2 x^2 - \xi^2 x^3} \quad (\text{B6})$$

The long dashed line in Fig. 16 shows the spectrum of photons for an unpolarized laser and the medium dashed line shows the photon spectrum with helicity  $-P_\gamma$ . Note that the most energetic photons are always polarized with opposite helicity to that of the laser photons.

## 2. Beamstrahlung Photons

The interpenetration of the dense electron and positron bunches in future  $e^+e^-$  colliders generates strong accelerations on the electrons and positrons near the interaction point which gives rise to synchrotron radiation which is referred to in the literature as beamstrahlung [19,20,21]. Beamstrahlung depends strongly on machine parameters such as luminosity, pulse rate, and bunch geometry. The distribution function of beamstrahlung photons can be written in the following approximation:

$$f_{\gamma/e}^{beam}(x, b) = f_{\gamma/e}^{(-)}(x, b) \Theta(x_c - x) + f_{\gamma/e}^{(+)}(x, b) \Theta(x - x_c) \quad (\text{B7})$$

where, as before,  $x$  is the fraction of the beam energy carried by the photon,  $b$  is the impact parameter of the produced  $\gamma$ , and  $x_c$  separates low and high photon energy regions where the different approximations to  $f_{\gamma/e}^{beam}(x, b)$  are used. The distribution used for small and intermediate values of  $x$  is given by

$$f_{\gamma/e}^{(-)}(x, b) \simeq \frac{CK}{\Upsilon^{1/3}} \left[ \frac{1 + (1-x)^2}{x^{2/3}(1-x)^{1/3}} \right] \left\{ 1 + \frac{1}{6C\Upsilon^{2/3}} \left( \frac{x}{1-x} \right)^{2/3} \exp \left[ \frac{2}{3\Upsilon} \frac{x}{(1-x)} \right] \right\}^{-1} \quad (\text{B8})$$

where  $C = -Ai'(0) = 0.2588$ , and  $Ai(x)$  is Airy's function. For large values of  $x$  the distribution is given by

$$f_{\gamma/e}^{(+)}(x, b) \simeq \frac{K}{2\sqrt{\pi}\Upsilon^{1/2}} \left[ \frac{1 - x(1-x)}{x^{1/2}(1-x)^{1/2}} \right] \exp \left[ -\frac{2}{3\Upsilon} \frac{x}{(1-x)} \right]. \quad (\text{B9})$$

The value  $x_c$  is such that  $f_{\gamma/e}^{beam}$  is continuous at  $x = x_c$ . It depends on the machine design; for the 500 GeV NLC,  $x_c \simeq 0.48$ . The dimensionless quantities  $K$  and  $\Upsilon$  are defined as

$$\begin{aligned} K &= 2\sqrt{3}\alpha \frac{\sigma_z E_\perp}{m} \\ \Upsilon &= \frac{pE_\perp}{m^3} \end{aligned} \quad (\text{B10})$$

where  $m$  and  $p$  are the electron mass and momentum, and  $E_\perp$  is the transverse electric field inside a uniform elliptical bunch of dimensions  $l_{x,y} = 2\sigma_{x,y}$  and  $l_z = 2\sqrt{3}\sigma_z$

$$E_\perp = \frac{N\alpha}{2\sqrt{3}(\sigma_x + \sigma_y)\sigma_z} \left( \frac{b_x^2}{\sigma_x^2} + \frac{b_y^2}{\sigma_y^2} \right)^{1/2} \quad (\text{B11})$$

with  $N$  being the number of particles in the bunch.

For the case of beamstrahlung we have to average over the impact parameter in addition to integrating over the energy fraction,  $x$ . Using elliptical coordinates the expression in the brackets of Eq. B11 becomes

$$\left( \frac{b_x^2}{\sigma_x^2} + \frac{b_y^2}{\sigma_y^2} \right)^{1/2} = 2b \quad (\text{B12})$$

and

$$f_{\gamma/e}^{beam}(x) = \int_0^1 f_{\gamma/e}^{beam}(x, b) 2b \, db \quad (\text{B13})$$

The photon luminosity of beamstrahlung is very sensitive to the transverse shape of the beam. The aspect ratio

$$G = \frac{\sigma_x + \sigma_y}{2\sqrt{\sigma_x\sigma_y}} \quad (\text{B14})$$

provides a good measure of beamstrahlung with large photon luminosities associated with small values of  $G$ . For high photon luminosity one tunes to round beams,  $G = 1$ . For the original NLC design  $G \simeq 2.7$ . We include the beam parameters for a number of NLC options in Table V.

### 3. Classical Bremstrahlung

Finally we consider conventional bremsstrahlung of photons by electrons which we use for the  $\sqrt{s} = 200$  GeV case and which also contributes to the photon luminosity when we consider beamstrahlung. We use the well-known Weizsäcker-Williams distribution [43] which we include for completeness:

$$f_{\gamma/e}^{WW}(x, E_{max}) = \frac{\alpha}{2\pi} \frac{1 + (1-x)^2}{x} \ln \left( \frac{E_{max}^2}{m_e^2} \right) \quad (\text{B15})$$

where  $E_{max}$  is the electron beam energy.

## REFERENCES

- [1] S.L. Glashow, Nucl. Phys. **22**, 579 (1961); S. Weinberg, Phys. Rev. Lett. **19**, 1264 (1967); A. Salam, Proc. of the 8th Nobel Symposium, ed. N. Svartholm (Willey, New York 1968).
- [2] C. Jarlskog, Proceedings of the XXV Conference on High Energy Physics, Singapore, August 1990 (World Scientific; 1991).
- [3] F. Dydak, Proceedings of the XXV Conference on High Energy Physics, Singapore, August 1990 (World Scientific; 1991).
- [4] J. Bagger, Proceedings of the 1991 TASI Institute, (World Scientific, Singapore, 1992).
- [5] A.F. Falk, M. Luke, and E.H. Simmons, Nucl. Phys. **B365**, 523 (1991); J. Bagger, S. Dawson, and G. Valencia, Fermilab-Pub-92/75-T; G. Valencia, Fermilab-Conf-92/246-T; F. Feruglio, University of Padova preprint, DFPD 92/TH/50 (1992, unpublished).
- [6] B. Holdom, Phys. Lett. **258B**, 156(1991).
- [7] B. Holdom and J. Terning, Phys. Lett. **247B**, 99 (1990); M. Peskin and T. Takeuchi, Phys. Rev. Lett. **65**, 964 (1990); G. Altarelli and R. Barbieri, Phys. Lett. **253B**, 161 (1991); D. Kennedy and P. Langacker, Phys. Rev. Lett. **65**, 2967 (1990); W.J. Marciano and J.L. Rosner, Phys. Rev. Lett. **65**, 2963 (1990).
- [8] K. Hagiwara, R. D. Peccei, D. Zeppenfeld, and K. Hikasa, Nucl. Phys. **B282**, 253 (1987).
- [9] K. Gaemers and G. Gounaris, Z. Phys. **C1**, 259 (1979); H. Aronson, Phys. Rev., **186**, 1434 (1969).
- [10] A. De Rújula *et al.*, Nucl. Phys. **B384**, 31 (1992); C.P. Burgess and D. London, McGill-92/04; McGill-92/05; K. Hagiwara *et al.*, Phys. Lett. **283B**, 353 (1992); C. Grosse-Knetter and R. Kögerler, Universität Bielefeld preprint BI-TP 92/56 (1992; unpublished).
- [11] UA2 Collaboration, J. Alitti *et al.*, Phys. Lett. **277B**, 194 (1992).
- [12] D. Zeppenfeld, Phys. Lett. **183B**, 380 (1987).



- [13] D. Treille *et al.*, Proceedings of the ECFA Workshop on LEP 200, ed. A. Böhm and W. Hoogland, Aachen (1986), CERN 87-08, vol. 2, p.414.
- [14] G.L. Kane, J. Vidal, and C.-P. Yuan, Phys. Rev. **D39**, 2617 (1989).
- [15] U. Baur and E.L. Berger, Phys. Rev. **D41**, 1476 (1990); J. Cortés, K. Hagiwara, and F. Herzog, Nucl. Phys. **B278**, 26 (1986); M. Samuel *et al.*, Phys. Rev. Lett. **67**, 9 (1991); N. Sinha, R. Sinha, and M.K. Sundaresan, Phys. Rev. **D44**, 2064 (1991)
- [16] C.H. Llewellyn-Smith and B. Wiik, DESY 77/36 (1977); P. Salati and J.C. Wallet, Z. Phys. **C16**, 155 (1982); A.N. Kamal *et al.*, Phys. Rev. **D24**, 2482 (1984); H. Neufeld, Z. Phys. **C17**, 145 (1983). G. Altarelli *et al.*, Nucl. Phys. **B262**, 204 (1985). E. Gabrielli, Mod. Phys. Lett. **A1**, 465 (1986). M. Böhm and A. Rosado, Z. Phys. **C39** 275 (1988); D. Atwood *et al.*, *W Production in ep Collisions*, Proceedings of the 1988 Snowmass Summer Study *High Energy Physics in the 1990's*, p. 264; U. Baur and D. Zeppenfeld, Nucl. Phys. **B325**, 253 (1989); D. Atwood *et al.*, *W Production at ep Colliders in the Process  $ep \rightarrow W^- \nu + X$* , Proceedings of the 1990 Summer Study on Research Directions for the Decade, Snowmass, Colorado, June 25 - July 13, 1990, (World Scientific, Singapore 1992); U. Baur and M.A. Doncheski, Phys. Rev. **D46**, 1959 (1992); T. Helbig and H. Spiesberger, Nucl. Phys. **B373**, 73 (1992); S. Godfrey, Z. Phys. **C55**, 619 (1992).
- [17] D. Zeppenfeld and S. Willenbrock, Phys. Rev. **D37**, 1775 (1988); U. Baur and D. Zeppenfeld, Phys. Lett. **201B**, 383 (1988); U. Baur and D. Zeppenfeld, Nucl. Phys. **B308**, 127 (1988).
- [18] I.F. Ginzburg *et al.*, Nucl. Instrum. Methods, **205**, 47 (1983); **219**, 5 (1984). C. Akerlof, Ann Arbor report UM HE 81-59 (1981; unpublished).
- [19] R. J. Noble, Nucl. Instrum. Methods **A256**, 427 (1987).
- [20] R. Blankenbecler and S.D. Drell, Phys. Rev. **D36**, 277 (1987); **D37**, 3308 (1988); Phys. Rev. Lett. **61**, 2324 (1988); R. Blankenbecler, S.D. Drell and N. Kroll, Phys. Rev. **D40**,

2462 (1989);

- [21] D. V. Schroeder, PhD Thesis, SLAC Report SLAC-371 (1990, unpublished).
- [22] H. König and K.A. Peterson, Phys. Lett. **B294**, 110 (1992); M.C. Gonzalez-Garcia, O.J.P. Éboli, F. Halzen, and S.F. Novaes, Phys. Lett. **B280**, 313 (1992); O.J.P. Éboli, M.C. Gonzalez-Garcia, F. Halzen, and S.F. Novaes, University of Wisconsin report MAD/PH/701 (1992, unpublished); K. Hagiwara, I. Watanabe, and P.M. Zerwas, Phys. Lett. **B278**, 187 (1992); E. Boos *et al.*, Phys. Lett. **B273**, 173 (1991); T. Kon, I. Ito, and Y. Chikashige, Phys. Lett. **B287**, 277 (1992); L. Bento and A. Mourao, Z. Phys. **C37**, 587 (1988); F. Cypers *et al.*, Nucl. Phys. **B383**, 45 (1992); A. Goto and T. Kon, Europhys. Lett. **19**, 575 (1992); B. Grzadkowski and J.F. Gunion, University of California Davis preprint, (1992; unpublished); J. E. Cieza Montalvo and O.J.P. Éboli, hep-ph bulletin board # 9208242 (1992; unpublished).
- [23] G. Couture, S. Godfrey, P. Kalyniak, Phys. Lett. **218B**, 361 (1989); Phys. Rev. **D39**, 3239 (1989); **D42**, 1841 (1990).
- [24] E. Yehudai, Phys. Rev. **D41**, 33 (1990); **D44**, 3434 (1991).
- [25] S.Y. Choi and F. Schrempp, Phys. Lett. **272B**, 149 (1991).
- [26] I.F. Ginzburg *et al.*, Nucl. Phys. **B228**, 285 (1983); K.O. Mikaelian, Phys. Rev., **D30**, 1115 (1984); F.M. Renard, Z. Phys. **C14**, 209 (1982); J.A. Robinson and T.G. Rizzo, Phys. Rev. **D33**, 2608 (1986); A. Denner and S. Dittmaier, CERN report CERN-TH.6585/92 (unpublished).
- [27] W.J. Marciano and A. Queijeiro, Phys. Rev. **D33**, 3449 (1986).
- [28] F. Boudjema, K. Hagiwara, C. Hamzaoui, and K. Numata, Phys. Rev. **D43**, 2223 (1991).
- [29] G. Couture and J. N. Ng. Z. Phys. **C35**, 65 (1987); E.N. Argyres *et al.*, CERN-TH.6510/92.

- [30] G. Couture *et al.*, Phys. Rev. **D38**, 860 (1988); T.M. Aliyev, Phys. Lett. **155B**, 364 (1985); S. Alam, S.N. Biswas, and A. Goyal, Phys. Rev. **D33**, 168 (1985).
- [31] J.-M. Freire, J.M. Moreno, M. Tytgat, and J. Orloff, CERN Report, CERN-TH.6573 (1992, unpublished).
- [32] R.S. Chivukula and M. Golden, Phys. Lett. **267B**, 233 (1991).
- [33] M. Suzuki, *Proceedings of the International Symposium on Bound Systems and Extended Objects*, Karuizawa Japan, March 19-21, 1992 (World Scientific, Singapore); M. Suzuki, Phys. Lett. **153B**, 289 (1985); T.G. Rizzo and M. A. Samuel, Phys. Rev. **D35**, 403 (1987).
- [34] J.M. Cornwall, D.N. Levin and G. Tiktopoulos, Phys. Rev. Lett. **30**, 1268 (1973); Phys. Rev. **D10**, 1145 (1974); C.H. Llewellyn Smith, Phys. Lett. **46B**, 233(1973); S.D. Joglekar, Ann. Phys. **83**, 427 (1974).
- [35] U. Baur and D. Zeppenfeld, Phys. Lett. **201B**, 383 (1988).
- [36] R. Kleiss and W.J. Stirling, Nucl. Phys. **B262** 235 (1985) and references therein.
- [37] See for example V. Barger and R. Phillips, *Collider Physics*, (Addison-Wesley Publishing Company, 1987).
- [38] H. Iwasaki, Inter. J. of Mod. Phys. **A7**, 3291 (1992); O. Philipsen, Zeit. Phys. **C54**, 643 (1992); K. Hagiwara *et al.*, Nucl. Phys. **B365**, 544 (1991); E.N. Argyres and C.G. Papadopoulos, Phys. Lett. **263B**, 298 (1991).
- [39] P. Kalyniak and P. Madsen, Carleton University report, in preparation; G. Couture, M. Gintner, and S. Godfrey, Carleton University report, in preparation;
- [40] Proceedings on *Physics and Experiments with Linear Colliders*, Lappland, Finland, 1991, edited by R. Orava.
- [41] R.B. Palmer, Ann. Rev. Nucl. Part. Sci. **40**, 529 (1990).

[42] These values are very rough estimates based on Monte Carlo studies. T. Barklow, private communications.

[43] C. Weizäcker, Z. Phys. **88** 612 (1934); E.J. Williams, Phys. Rev. **45**, 729 (1934).

## FIGURES

FIG. 1. Feynman diagram for the  $WW\gamma$  vertex corresponding to the Lagrangian and Feynman rule given in the text.

FIG. 2. The Feynman diagrams contributing to the process  $e\gamma \rightarrow \nu q\bar{q}$ . For the process  $e\gamma \rightarrow \nu_e\mu\bar{\nu}_\mu$  diagram (c) does not contribute and the quark charge in diagram (d) should be replaced by the  $\mu$  charge.

FIG. 3. The angular distributions of the outgoing  $W$  boson relative to the incoming electron for  $\sqrt{s} = 120$  GeV. In fig. (a) there is no photon distribution folded in (so the process is in the  $e\gamma$  centre of mass) while in fig. (b) the backscattered laser photon distribution is included. In both cases the solid line is the standard model prediction, the long-dashed line is for  $\kappa_\gamma = -1$ ,  $\lambda_\gamma = 0$ , the short-dashed line is for  $\kappa_\gamma = 2$ ,  $\lambda_\gamma = 0$ , and the dotted line is for  $\kappa_\gamma = 1$ ,  $\lambda_\gamma = 2$ .

FIG. 4. The achievable bounds on  $\kappa_\gamma$  and  $\lambda_\gamma$  at 95% C.L. using the hadronic decay mode of the  $W$  boson for the  $\sqrt{s} = 120$  GeV collider described in the text. Fig. (a) is for  $L = 100$  pb $^{-1}$  and fig. (b) is for  $L = 500$  pb $^{-1}$ . In both cases the dotted line is derived from measurements of the total cross section ( $\sigma_T$ ), the dashed line from  $A_{FB}$ , the dot-dashed line from  $R_{13}$  and the solid line from combining  $\sigma_T$  and  $A_{FB}$ .

FIG. 5. The angular distributions of the outgoing  $W$  boson relative to the incoming electron for  $\sqrt{s} = 200$  GeV using the Weizacker-Williams effective photon distribution. The solid line is the standard model prediction, the long-dashed line is for  $\kappa_\gamma = -1$ ,  $\lambda_\gamma = 0$ , the short-dashed line is for  $\kappa_\gamma = 2$ ,  $\lambda_\gamma = 0$ , and the dotted line is for  $\kappa_\gamma = 1$ ,  $\lambda_\gamma = 2$ .

FIG. 6. The achievable bounds on  $\kappa_\gamma$  and  $\lambda_\gamma$  at 95% C.L. for a  $\sqrt{s} = 200$  GeV  $e^+e^-$  collider using the hadronic decay mode of the  $W$  boson. Fig. (a) is for  $L = 100$  pb $^{-1}$  and fig. (b) is for  $L = 500$  pb $^{-1}$ . In both cases the dotted line is derived from measurements of the total cross section ( $\sigma_T$ ), the dashed line from  $A_{FB}$  and the solid line from combining the measurements.

FIG. 7. The invariant mass distributions of the hadronic jets coming from hadronic  $W$  decay for  $\sqrt{s} = 200$  GeV using the Weizacker-Williams effective photon distribution. The solid line is the standard model prediction, the long-dashed line is for  $\kappa_\gamma = -1$ ,  $\lambda_\gamma = 0$ , the short-dashed line is for  $\kappa_\gamma = 2$ ,  $\lambda_\gamma = 0$ , and the dotted line is for  $\kappa_\gamma = 1$ ,  $\lambda_\gamma = 2$ .

FIG. 8. The angular distributions of the outgoing muon and reconstructed  $W$  boson relative to the incoming electron for  $\sqrt{s} = 500$  GeV. (a) For a muon with the backscattered laser photon spectrum, (b) for a muon with the beamstrahlung photon spectrum, (c) for a reconstructed  $W$  boson with the backscattered laser photon spectrum, and (d) for a  $W$  boson with the beamstrahlung photon spectrum. In all cases the solid line is the standard model prediction, the long-dashed line is for  $\kappa_\gamma = 0.6$ ,  $\lambda_\gamma = 0$ , the short-dashed line is for  $\kappa_\gamma = 1.4$ ,  $\lambda_\gamma = 0$ , and the dotted line is for  $\kappa_\gamma = 1$ ,  $\lambda_\gamma = 0.4$ .

FIG. 9. The  $p_T$  distributions of the outgoing muon and reconstructed  $W$  boson for  $\sqrt{s} = 500$  GeV with the same labelling as in Fig. 8.

FIG. 10. The hadron jet invariant mass ( $M_{q\bar{q}}$ ) distribution for  $\sqrt{s} = 500$  GeV. (a) For the backscattered laser photon spectrum and (b) for the beamstrahlung photon spectrum. In both cases the solid line is the standard model prediction, the long-dashed line is for  $\kappa_\gamma = 0.6$ ,  $\lambda_\gamma = 0$ , the short-dashed line is for  $\kappa_\gamma = 1.4$ ,  $\lambda_\gamma = 0$ , and the dotted line is for  $\kappa_\gamma = 1$ ,  $\lambda_\gamma = 0.4$ .

FIG. 11. The achievable bounds on  $\kappa_\gamma$  and  $\lambda_\gamma$  at 95% C.L. for a  $\sqrt{s} = 500$  GeV  $e^+e^-$  collider (a) using a backscattered laser photon spectrum (b) using a beamstrahlung photon spectrum. In both cases the dashed line is based on the angular distribution divided into four bins, the dotted line is based on the  $p_T$  distribution of the  $W$  boson divided into the four bins given in the text, the dot-dashed line is for  $\sigma_{q\bar{q}} > 300$  GeV and the solid line is the combined angular and  $p_T$  bounds.

FIG. 12. The angular distributions of the outgoing muon and reconstructed  $W$  boson relative to the incoming electron for  $\sqrt{s} = 1$  TeV. (a) For a muon with the backscattered laser photon spectrum, (b) for a muon with the beamstrahlung photon spectrum, (c) for a reconstructed  $W$  boson with the backscattered laser photon spectrum, and (d) for a  $W$  boson with the beamstrahlung photon spectrum. In all cases the solid line is the standard model prediction, the long-dashed line is for  $\kappa_\gamma = 0.6$ ,  $\lambda_\gamma = 0$ , the short-dashed line is for  $\kappa_\gamma = 1.4$ ,  $\lambda_\gamma = 0$ , and the dotted line is for  $\kappa_\gamma = 1$ ,  $\lambda_\gamma = 0.1$ .

FIG. 13. The  $p_T$  distributions of the outgoing muon and reconstructed  $W$  boson for  $\sqrt{s} = 1$  TeV with the same labelling as Fig. 12.

FIG. 14. The achievable bounds on  $\kappa_\gamma$  and  $\lambda_\gamma$  at 95% C.L. for a  $\sqrt{s} = 1$  TeV  $e^+e^-$  collider with the same line definitions as Fig. 11 except here the dot-dashed line is for  $\sigma_{q\bar{q}} > 600$  GeV

FIG. 15. The  $p_T$  distribution for the  $\mu$  for different values of  $\Lambda$ , the energy scale in the anomalous couplings form factor. The short dashed line is for  $\Lambda = 500$  GeV, the solid line for  $\Lambda = 1$  TeV, and the dashed line for  $\Lambda = 2$  TeV.

FIG. 16. The photon distributions described in the text. The solid line is the Weizacker-Williams distribution, the long dashed line is the backscattered photon distribution, the medium dashed line is the backscattered photon distribution for photons with opposite polarization to that of the laser, the short dashed line is the backscattered photon distribution for photons with the same polarization as the laser, the dotted line is the beamstrahlung spectrum for  $\sqrt{s} = 500$  GeV with  $G=2.7$ , and the dash-dot line is with  $G=1$ .

# TABLES

TABLE I. Bounds on  $\kappa_\gamma$  and  $\lambda_\gamma$  from a 120 GeV  $e^+e^-$  collider using a backscattered laser photon distribution.

		$\delta\kappa_\gamma$			$\delta\lambda_\gamma$		
		68% C.L.	90 % C.L.	95 % C.L.	68% C.L.	90 % C.L.	95 % C.L.
$\sigma_W$	L=100 pb <sup>-1</sup>	+0.10 -0.11	+0.16 -0.19	+0.18 -0.23	+0.8 -0.8	+1.1 -1.1	+1.2 -1.2
	L=500 pb <sup>-1</sup>	+0.04 -0.05	+0.07 -0.08	+0.08 -0.09	+0.5 -0.6	+0.7 -0.7	+0.8 -0.8
$A_{FB}$	L=100 pb <sup>-1</sup>	weak bounds			+1.0 -1.0	+1.4 -1.4	+1.6 -1.6
	L=500 pb <sup>-1</sup>	weak bounds			+0.6 -0.7	+0.8 -0.9	+0.9 -1.0
$R_{13}$	L=100 pb <sup>-1</sup>	weak bounds			+0.8 -2.1	+1.3 -3.0	+1.6 -3.8
	L=500 pb <sup>-1</sup>	weak bounds			+0.4 -1.5	+0.6 -1.8	+0.7 -2.0
$\sigma_F + \sigma_B$	L=100 pb <sup>-1</sup>	+0.16 -0.19	+0.20 -0.26	+0.23 -0.30	+0.9 -1.0	+1.1 -1.1	+1.2 -1.2
	L=500 pb <sup>-1</sup>	+0.07 -0.08	+0.09 -0.10	+0.11 -0.12	+0.6 -0.6	+0.7 -0.7	+0.8 -0.8



TABLE II. Bounds on  $\kappa_\gamma$  and  $\lambda_\gamma$  from the process  $e^+e^- \rightarrow e^+W^- \rightarrow e^+q\bar{q}$  at  $\sqrt{s} = 200$  GeV in the Weizacker-Williams approximation.

		$\delta\kappa_\gamma$			$\delta\lambda_\gamma$		
		68% C.L.	90 % C.L.	95 % C.L.	68% C.L.	90 % C.L.	95 % C.L.
$\sigma_W$	L=100 pb <sup>-1</sup>	+0.14 -0.17	+0.23 -0.29	+0.27 -0.36	+0.6 -0.7	+0.8 -0.9	+0.9 -1.0
	L=500 pb <sup>-1</sup>	+0.06 -0.07	+0.11 -0.12	+0.13 -0.15	+0.4 -0.4	+0.5 -0.6	+0.6 -0.6
$A_{FB}$	L=100 pb <sup>-1</sup>	weak bounds			+1.0 -1.0	+1.4 -1.5	+1.7 -1.7
	L=500 pb <sup>-1</sup>	weak bounds			+0.6 -0.6	+0.8 -0.8	+0.9 -0.9
$\sigma_F + \sigma_B$	L=100 pb <sup>-1</sup>	+0.23 -0.30	+0.3 -0.4	+0.3 -0.5	+0.8 -0.8	+0.9 -0.9	+0.9 -1.0
	L=500 pb <sup>-1</sup>	+0.11 -0.12	+0.14 -0.16	+0.16 -0.18	+0.5 -0.5	+0.6 -0.6	+0.6 -0.6

TABLE III. Bounds on  $\kappa_\gamma$  and  $\lambda_\gamma$  from the processes  $e^-\gamma \rightarrow \mu^-\bar{\nu}_\mu\nu_e$  and  $e^-\gamma \rightarrow W^- \rightarrow e^+q\bar{q}$  at  $\sqrt{s} = 500$  using backscattered laser photon distributions (laser) and beamstrahlung photon distributions (beam). The  $\sigma_{q\bar{q}}^a$  results are for the hadron mode with  $M_{q\bar{q}} > 100$  GeV and the  $\sigma_{q\bar{q}}^b$  results are for the hadron mode with  $M_{q\bar{q}} > 300$  GeV.

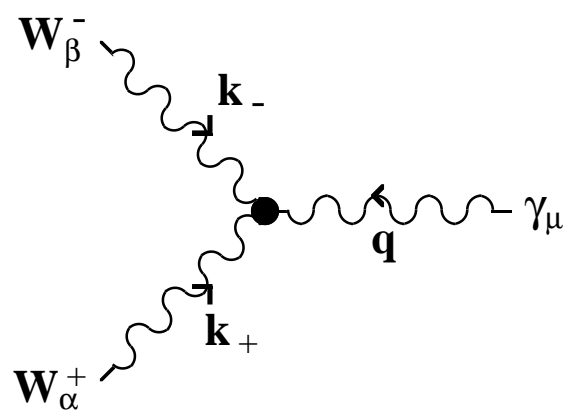
		$\delta\kappa_\gamma$			$\delta\lambda_\gamma$		
		68% C.L.	90 % C.L.	95 % C.L.	68% C.L.	90 % C.L.	95 % C.L.
$\sqrt{s} = 500$ GeV							
$\sigma_W$	laser	+0.05 -0.05	+0.08 -0.08	+0.09 -0.10	+0.14 -0.15	+0.18 -0.19	+0.20 -0.21
	beam	+0.04 -0.04	+0.07 -0.07	+0.08 -0.09	weak bounds		
$\sigma_\mu$	laser	+0.05 -0.05	+0.08 -0.08	+0.09 -0.10	+0.15 -0.15	+0.19 -0.20	+0.21 -0.21
	beam	+0.04 -0.05	+0.07 -0.08	+0.09 -0.09	weak bounds		
$\cos\theta_W$	laser	+0.05 -0.05	+0.06 -0.07	+0.07 -0.07	+0.09 -0.09	+0.10 -0.10	+0.10 -0.11
	beam	+0.05 -0.05	+0.06 -0.06	+0.07 -0.07	weak bounds		
$p_{T_W}$	laser	+0.05 -0.05	+0.06 -0.07	+0.07 -0.08	+0.04 -0.04	+0.05 -0.05	+0.05 -0.05
	beam	+0.05 -0.06	+0.06 -0.07	+0.07 -0.08	+0.05 -0.05	+0.05 -0.05	+0.06 -0.06
$\sigma_{q\bar{q}}^a$	laser	+0.04 -0.04	+0.07 -0.07	+0.08 -0.09	+0.12 -0.07	+0.15 -0.09	+0.16 -0.10
	beam	+0.04 -0.05	+0.07 -0.08	+0.08 -0.10	+0.19 -0.10	+0.23 -0.14	+0.24 -0.16
$\sigma_{q\bar{q}}^b$	laser	weak bounds			+0.07 -0.05	+0.09 -0.06	+0.10 -0.07
	beam	weak bounds			+0.12 -0.09	+0.14 -0.12	+0.16 -0.13

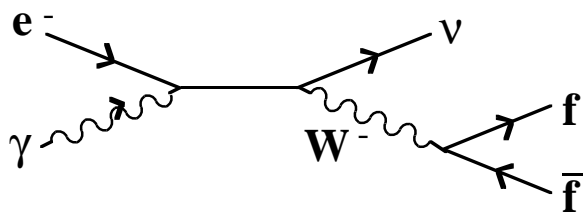
TABLE IV. Bounds on  $\kappa_\gamma$  and  $\lambda_\gamma$  from the processes  $e^-\gamma \rightarrow \mu^-\bar{\nu}_\mu\nu_e$  and  $e^-\gamma \rightarrow W^- \rightarrow e^+q\bar{q}$  at 1 TeV using backscattered laser photon distributions (laser) and beamstrahlung photon distributions (beam). The  $\sigma_{q\bar{q}}$  results are for the hadron mode with  $M_{q\bar{q}} > 600$  GeV.

		$\delta\kappa_\gamma$			$\delta\lambda_\gamma$		
		68% C.L.	90 % C.L.	95 % C.L.	68% C.L.	90 % C.L.	95 % C.L.
$\sqrt{s} = 1$ TeV							
$\sigma_W$	laser	+0.05 -0.05	+0.08 -0.09	+0.09 -0.10	+0.07 -0.08	+0.09 -0.10	+0.10 -0.11
	beam	+0.05 -0.05	+0.08 -0.08	+0.09 -0.10		weak bounds	
$\sigma_\mu$	laser	+0.05 -0.05	+0.08 -0.09	+0.09 -0.10	+0.08 -0.08	+0.10 -0.10	+0.11 -0.12
	beam	+0.05 -0.05	+0.08 -0.08	+0.09 -0.10		weak bounds	
$\cos\theta_W$	laser	+0.05 -0.06	+0.06 -0.07	+0.07 -0.08	+0.04 -0.04	+0.05 -0.05	+0.05 -0.05
	beam	+0.05 -0.05	+0.06 -0.07	+0.07 -0.08		weak bounds	
$p_{T_W}$	laser	+0.05 -0.07	+0.06 -0.10	+0.07 -0.11	+0.013 -0.013	+0.015 -0.015	+0.016 -0.016
	beam	+0.05 -0.07	+0.06 -0.10	+0.07 -0.12	+0.015 -0.015	+0.017 -0.017	+0.018 -0.018
$\sigma_{q\bar{q}}$	laser		weak bounds		+0.025 -0.017	+0.031 -0.023	+0.03 -0.03
	beam		weak bounds		+0.03 -0.03	+0.04 -0.04	+0.05 -0.04

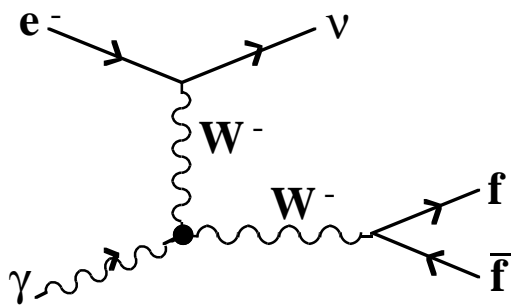
TABLE V. NLC Machine Parameters

	NLC		TLC	
$E_{cm}$ (TeV)	0.5	0.5	1	1
$L$ (cm <sup>-2</sup> sec <sup>-1</sup> )	$9 \times 10^{33}$			
$N$	$1.67 \times 10^{10}$	$1.67 \times 10^{10}$	$1.67 \times 10^{10}$	$1.67 \times 10^{10}$
$\sigma_z$ (cm)	0.011	0.011	0.011	0.011
$\sigma_y$ (cm)	$6.5 \times 10^{-7}$	$3.3 \times 10^{-6}$	$1.7 \times 10^{-5}$	$3.3 \times 10^{-6}$
$\sigma_x$ (cm)	$1.7 \times 10^{-5}$	$3.3 \times 10^{-6}$	$1.7 \times 10^{-5}$	$3.3 \times 10^{-6}$
G	2.7	1.0	2.7	1.0
$x_c$	0.48	0.64	0.58	0.72

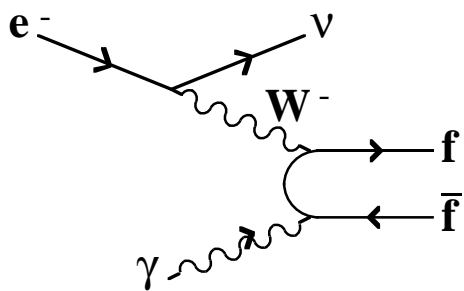




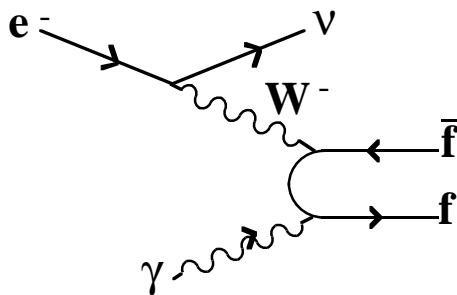
a)



b)



c)



d)

